

Compression Deformation Mechanisms at the Nanoscale in Magnesium Single Crystal

Yafang GUO¹†, Xiaozhi TANG¹, Yuesheng WANG¹, Zhengdao WANG¹ and Sidney YIP²

1) Institute of Engineering Mechanics, Beijing Jiaotong University, Beijing 100044, China

2) Department of Nuclear Science and Engineering, Massachusetts Institute of Technology, Cambridge, Massachusetts 02139, USA

[Manuscript received 7 August 2012, in revised form 17 October 2012]

© The Chinese Society for Metals and Springer-Verlag Berlin Heidelberg

The dominant deformation mode at low temperatures for magnesium and its alloys is generally regarded to be twinning because of the hcp crystal structure. More recently, the phenomenon of a “loss” of the twins has been reported in microcompression experiments of the magnesium single crystals. Molecular dynamics simulation of compression deformation shows that the pyramidal $\langle a + c \rangle$ slip dominates compression behavior at the nanoscale. No compression twins are observed at different temperatures at different loadings and boundary conditions. This is explained by the analyses, that is, the $\{10\bar{1}2\}$ and $\{10\bar{1}1\}$ twins can be activated under c -axis tension, while compression twins will not occur when the c/a ratio of the hcp metal is below $\sqrt{3}$. Our theoretical and simulation results are consistent with recent microcompression experiments of the magnesium (0001) single crystals.

KEY WORDS: Magnesium; Compression; Slip; Molecular dynamics simulation

1. Introduction

Magnesium and its alloys are of interest for automotive and aerospace applications due to their low densities ($\sim 1.74 \text{ g/cm}^3$) and relatively high specific strength. However, the plastic deformation mechanisms of magnesium are not well understood. From the mechanical point of view, magnesium and its wrought alloys show a pronounced direction-dependence of plastic yielding and work hardening, as well as different yielding behavior in tension and compression, the so-called strength differential (SD) effect^[1]. This feature is due to the hcp structure of magnesium. Compared to the fcc metals, the number of slip systems allowing plastic deformation in magnesium are limited, which in turn favor deformation by twinning. Two types of twins are frequently reported in magnesium alloys: $\{10\bar{1}2\}\langle 10\bar{1}1 \rangle$ c -axis tension

twins^[1–3] and $\{10\bar{1}1\}\langle 10\bar{1}2 \rangle$ c -axis compression twins^[4–6]. The critical resolved shear stress (CRSS) for the tension twin is lower than that of the compression twin^[7]. Thus the former occurs more easily, which is often thought to have a favorable effect on the ductility of the magnesium alloys.

Besides twinning, shear bands are also widely observed in the experiments on magnesium and its alloys^[8–10]. For some cold rolled magnesium alloys examined by electron backscatter diffraction (EBSD), the dominant features of the microstructure are characterized by both twins and shear bands^[9]. The shear bands are suggested to be favorable in rolling deformation for magnesium, and it is proposed that the cold rollability seen in certain specimens arises from the presence of “soft” banded regions^[10], which may be regarded as “compression bands”^[1]. Experimental observations^[9] have additionally revealed the volume fraction of the shear bands increases with increasing strain, while that of the twins decrease. The phenomenon of a “loss” of twins seems to appear with increasing rolling reduction.

In recent years, observation of “loss” of twins in

† Corresponding author. Prof., Ph.D.; Tel: +86 10 51682094; Fax: +86 10 51682094; E-mail address: yfguo@bjtu.edu.cn (Yafang GUO)

microcompression experiments for magnesium single crystals has been facilitated by improvements in experiment techniques. Microcompression measurements of the single crystal FIB columns on (0001) magnesium showed that no twinning could be observed in the sample sizes from 2.1 to 10 μm under *c*-axis compression^[11]. In this case significant plasticity and hardening occurred due to six active pyramidal $\pi 2$ slip systems, and there was appreciable size effect in the flow strength, the smaller being stronger. Meanwhile, TEM analysis of micropillar specimens of magnesium single crystals confirmed that no deformation twinning was observed in compression along the [0001] *c*-axis^[12]. Multiple slip systems become active on the pyramidal planes, resulting in significant hardening for length scales from 2.1 to 10 μm . These results point to an intriguing deformation pattern of magnesium single crystal at the nanoscale, namely no deformation twins are present in the microcompression deformed specimens. This is in contrast to observations on bulk samples indicating the deformation twinning is the primary mechanism for *c*-axis compression^[4,5]. Additionally, a strong crystal size effect on deformation twinning in hcp titanium has been reported^[13]. Using microcompression and in situ nano-compression measurements, it was found that the stress required for deformation twinning increases drastically with decreasing sample size of a titanium alloy single crystal. When the crystal sample size is below 1 μm , deformation twinning was entirely replaced by dislocation plasticity. These experimental results revealed the ‘loss’ of twin phenomenon in hcp metals at the nanoscale, and a strong size effect on deformation twinning.

Deformation mechanism acted in magnesium and its alloys still remain open. Besides experimental techniques, atomistic simulations can contribute to clarifying the competing deformation mechanism by providing explicit details on atomic displacements. In molecular dynamics (MD) simulation, an ideal ma-

terial model can be established without the complications of unavoidable defects in real materials. Under such conditions the elementary mechanism of crack propagation, dislocation dynamics, structural phase transformation, and the strength of nanocrystalline solids have been revealed^[14–19]. For magnesium, the mechanism for the most commonly observed $\{10\bar{1}2\}$ deformation twinning were uncovered by atomistic simulations^[20,21]. Moreover, the elementary twinning dislocations (TDs) for $\{\bar{1}011\}$ and $\{\bar{1}013\}$ twins are identified by atomic-scale computer simulations^[22,23]. In previous work, the deformation behavior in magnesium single crystal under *c*-axis tension was investigated through atomistic simulations^[24]. At low temperatures, twinning was found to be the main deformation mechanism. It is notable that the $\{10\bar{1}2\}$ ($\pi 3$) tension and $\{10\bar{1}1\}$ ($\pi 1$) compression twinning were both observed in this simulation of *c*-axis tension.

In order to obtain further understanding of deformation mechanism in pure magnesium, atomistic simulations of single crystals are carried out in the present work to investigate *c*-axis compression deformation behavior at the nanoscale. The deformation mechanism of pure magnesium single crystal at different temperatures is studied using different loading and boundary conditions. We find the main deformation mechanism under *c*-axis compression to be pyramidal slip rather than twinning. This agrees well with recent microcompression measurements of single crystal magnesium^[11,12].

2. Setup of MD Simulation

In Fig. 1, the lattice structure of the hcp crystal and its orientation are shown. In Fig. 1(b), the atomic positions in a hcp crystal (*c/a* is 1.623) are shown. It can be seen that the atoms align in layers along the $[\bar{1}2\bar{1}0]$ direction periodically with the sequence of $\cdots ABAB \cdots$: atoms in layer A are marked

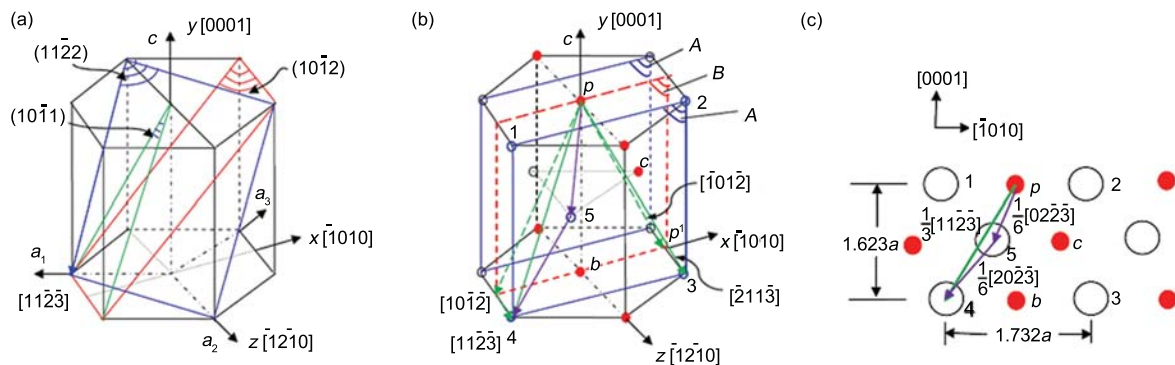


Fig. 1 Lattice structure of hcp crystal: (a) three pyramidal slip planes $\pi 3$ $\{10\bar{1}2\}$ (in red), $\pi 1$ $\{10\bar{1}1\}$ (in green), and $\pi 2$ $\{11\bar{2}2\}$ (in blue) are shown; (b) periodic arrangement of atoms along the $[\bar{1}2\bar{1}0]$ direction with the sequence of $\cdots ABAB \cdots$; (c) atoms arrangement in a plane representation, including atoms in both A and B layers projected in one $[\bar{1}2\bar{1}0]$ plane

as black open circles, and atoms in layer *B* as red close circles. Thus, the atomic arrangement can be projected in one $(\bar{1}2\bar{1}0)$ plane, including atoms in layer *A* and *B*, as shown in Fig. 1(c).

A plane strain condition is considered in order to reduce the computational cost compared to a full 3D simulation, with a periodic boundary condition applied in the $(\bar{1}2\bar{1}0)$ (*z*) direction. Four outermost layers of the atoms in the top and bottom sides of the model are assigned to represent the boundary region, shown in Fig. 2 as grey regions. The thickness of the boundary region is chosen to be larger than the cut-off distance of the potential adopted for the simulation, an EAM potential for magnesium developed by Liu *et al.*^[25] by fitting both the ab initio forces and experimental data on various bulk structural properties^[21,25,26]. The XMD program^[27] is used for the atomistic simulations.

Initial configurations of perfect magnesium single crystal samples are first defined in the simulations. Then different loading and boundary conditions are applied as described in section 3. Several systems of different sizes were tested beforehand. It was verified that the basic results of the structure evolution in the simulations are not affected by the presence of the fixed boundary, nor are they sensitive to the system size once the atomistic region has reached sufficient dimensions. Results will be presented for the systems of dimensions 27 nm × 48 nm × 2.5 nm containing 160000 atoms, and 22 nm × 29 nm × 2.5 nm containing 76800 atoms. System temperature is kept constant during the simulation by scaling the instantaneous velocities of all atoms with the appropriate Maxwell-Boltzmann distribution at a specified temperature.

3. Results and Analysis

3.1 Deformation behavior of the magnesium single crystal under quasi-static compression

We begin with a quasi-static simulation of *c*-axis compression. After the initial configurations of the single crystal samples are obtained, all atoms are shifted to the positions specified by different values of strain along the *c*-axis (*y* direction). Then the atoms are fully relaxed for 10000 steps, each of magnitude 6×10^{-15} s, and the evolution of the atomic positions in the crystals at different loading levels is determined. During relaxation free boundary condition is applied in the $(\bar{1}010)$ (*x*) direction, periodic boundary condition is applied in the $(\bar{1}2\bar{1}0)$ (*z*) direction, and fixed-displacement boundary condition is applied in the *x* and *y* directions for the boundary region. After imposing strain in increments, it is found that deformation is clearly observed when the value of strain reaches 0.08. Therefore we will focus on the deformation results at a compressive strain of 0.08 as shown in Fig. 2.

Fig. 2 shows the deformation of the magnesium single crystal under *c*-axis compression at different temperatures. The atoms in these pictures are shown in a plane representation, two different $(\bar{1}2\bar{1}0)$ planes (layer *A* and layer *B* as shown in Fig. 1(b)) are presented. Localized displacements along definite directions in the form of slip bands are observed in these plane representations at all three temperatures, with more and broader slip bands being activated with increasing temperature. Fig. 3 gives the detailed atomic structures of the slip bands by showing a plane

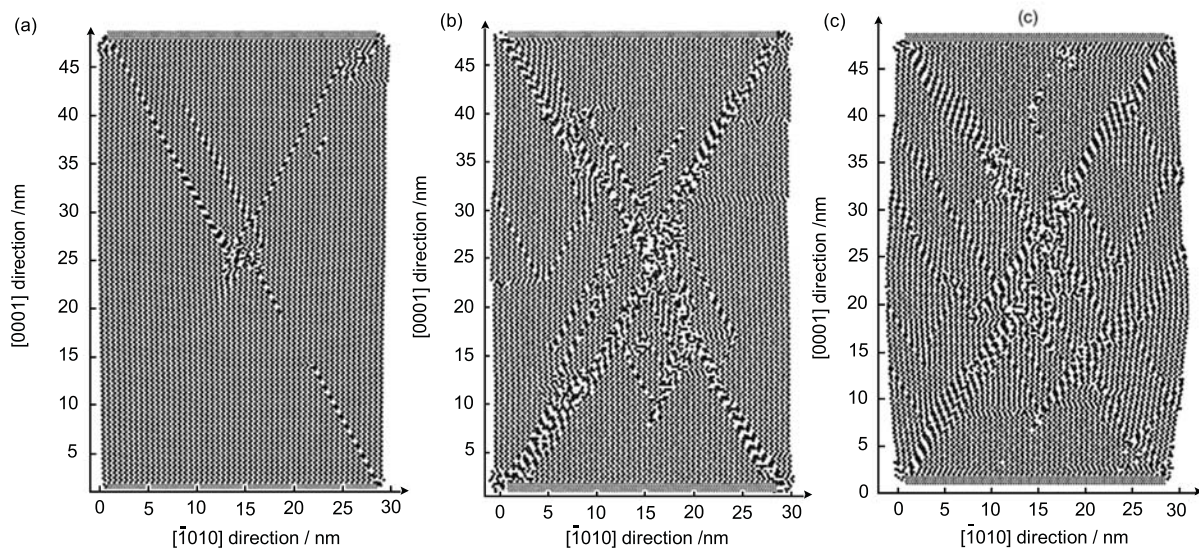


Fig. 2 Deformation of magnesium single crystal under *c*-axis compression at 5 K (a), 298 K (b), and 500 K (c) at a compression strain of 0.08. The atoms in these pictures are shown in a plane representation, two different $(\bar{1}2\bar{1}0)$ planes (layer *A* and layer *B* as shown in Fig. 1(b)) are presented. Free-boundary condition is applied in the $(\bar{1}010)$ direction. Localized displacements along definite directions in the form of slip bands are observed at all three temperatures, with more and broader slip bands being activated with increasing temperature

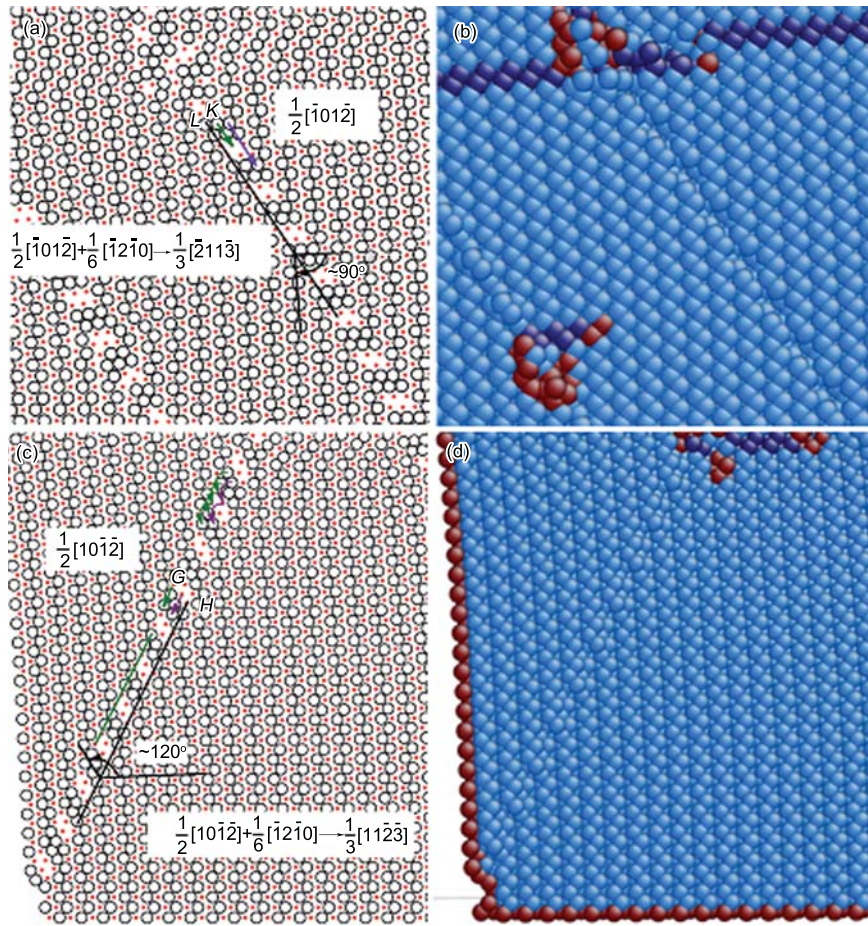


Fig. 3 Atomic arrangements in the slip bands: (a) and (c), plane representations of two typical types of shear region. Two different $(\bar{1}2\bar{1}0)$ planes (layer A and layer B) are projected in one plane. Only the atoms movement projected in the $(\bar{1}2\bar{1}0)$ plane can be shown, while the atoms movement along the $[\bar{1}2\bar{1}0]$ periodic direction will not be visible; (b) and (d), corresponding atoms represented by the CNA 22 (light blue is for perfect atoms, dark blue for atoms in fcc structure and red for atoms with other structures. See text for discussion)

representation and atoms identified according to the method of common neighbor analysis (CNA)^[28]. In CNA method a decomposition of the radial distribution function according to the local environment of the pairs of atoms enables direct interpretation of the various features of the radial distribution function in terms of atomic structure. It can be used to identify atoms in particular local environments, such as fcc, hcp, bcc or certain defects^[29–31]. If we define a reorientation angle between the original matrix and the slipped volume on the basis of atoms arrangement, similar to that in twins, two typical slip bands are found in Fig. 2. One is the slip band with the reorientation angle of about 90° as shown in Fig. 3(a), and the other is with the reorientation angle of about 120° as shown in Fig. 3(c). In the corresponding CAN in Fig. 3(b) and (d), colors are assigned to the atoms according to their local crystal structures: light blue for perfect atoms, dark blue for the atoms in fcc structures and the red for the atoms with other structures. It is found in Fig. 3(b) and (d) that no defect is observed in the slip region, except a step associated with atoms in different $(\bar{1}2\bar{1}0)$ layers. It means that no

structural defect is formed due to the slip, although the shear can be observed in the plane representations as shown in Fig. 3(a) and (c). The slip bands shown in Fig. 3(b) and (d) have a perfect hcp structure, just as their neighbor regions. Meanwhile, some interior defects are left behind at the end of the slip region, shown as red and dark blue, and a slip step appears at the surface as shown in Fig. 3(d).

In order to find the reason why no defect exists in the slip region as shown in Figs. 3(b) and (d), we checked the atomic movements carefully. It is found that beside shear along the $[\bar{1}01\bar{2}]$ direction as shown in Fig. 3(a), the atoms in the slip region also move along the $[\bar{1}2\bar{1}0]$ periodic direction. In Fig. 3(a), a plane representation is shown. Only movement of the atoms projected onto the $(\bar{1}2\bar{1}0)$ plane along the $[\bar{1}01\bar{2}]$ direction from point p to point p' shown in Fig. 1(b) are represented, the movement along the $[\bar{1}2\bar{1}0]$ periodic direction from point p' to point 3 are not visible. Suppose we consider the displacement along the $[\bar{1}2\bar{1}0]$ direction ($\frac{1}{2}[\bar{1}01\bar{2}] + \frac{1}{6}[\bar{1}2\bar{1}0] \rightarrow \frac{1}{3}[\bar{2}11\bar{3}]$), in which the atoms undergo a pyramidal $\langle a+c \rangle$ slip of $\frac{1}{3}[\bar{2}11\bar{3}]$ from point p to point 3 moving

from layer B to layer A (red atoms changing to white circles as shown in solid green line in Fig. 1(b)). In Fig. 3(a), we define the slip plane as a solid black line L in the plane representation, which is the boundary between slip region and nonslip region. It is observed that the atoms in the neighboring plane K slip a vector of $\frac{1}{3}[\bar{2}11\bar{3}]$ (only the vector of $\frac{1}{2}[\bar{1}01\bar{2}]$ is shown as the green arrow line), while atoms move from layer B to layer A . Moreover, a double $\frac{1}{3}[\bar{2}11\bar{3}]$ slip (purple arrow line) occurs for atoms on the right of the plane K , while the type of atoms has not changed.

If considering the displacements along the $[\bar{1}2\bar{1}0]$ periodic direction in the plane representation in Fig. 3(a), we exchange the type of the atoms along the plane K (that is, change black circles to green dots, and red dots to blue circles in Fig. 4(a)), then the slip band disappears in this plane representation and a perfect hcp structure is recovered as shown in Fig. 4(b). This is exactly the same as the CNA representation in Fig. 3(b). It means that no structural defect is formed in the slip region after the pyramidal slip, although the shear can be clearly observed in a plane representation.

For the slip band with the reorientation angle of about 120° in Fig. 3(c), a pyramidal $\frac{1}{3}[11\bar{2}\bar{3}]$ slip occurs for the atoms on the plane G (shown as green lines). Of course, only the vector of $\frac{1}{2}[10\bar{1}\bar{2}]$ is shown as the green arrow line in this plane representation. Meanwhile, all atoms on the left of plane G (including plane G) move from layer B to layer A , and the Burgers vector is $\frac{1}{3}[11\bar{2}\bar{3}]$. However, for the atoms between the planes G and the slip plane H , only one layer of atoms move a vector $\frac{1}{3}[11\bar{2}\bar{3}]$ (shown as purple arc lines), while the other layer of atoms do not move. Therefore, after the $\frac{1}{3}[11\bar{2}\bar{3}]$ slips in different planes, the slip band still has the perfect hcp structure, as

shown in Fig. 3(d). No twinning with symmetrical structure has been found. We can only observe a slip step at the surface of the simulation cell, and some interior defects left behind at the end of the shear region. In Fig. 3(b) and (d), the dark blue indicates atoms in fcc structure. The red indicates other defects, including the free surface and some complicated interior defects caused by dislocation interactions.

We have carefully examined the stepwise dynamic response of the deformation, and observed the nucleation of dislocations at the free surface and at the interior defect, separately. It is found that a full pyramidal slip of $\frac{1}{3}[11\bar{2}\bar{3}]$ is accomplished by two steps, the first step is a $\frac{1}{6}[20\bar{2}\bar{3}]$ slip, and then followed by a $\frac{1}{6}[0\bar{2}\bar{2}\bar{3}]$ slip, shown as purple line in Fig. 1(b) and (c). After the first step of a $\frac{1}{6}[20\bar{2}\bar{3}]$ slip, a stacking fault is formed as shown in Fig. 5. The purple circle in Fig. 5(a) shows the core of $\frac{1}{6}[20\bar{2}\bar{3}]$ partial dislocation. When the second step is accomplished, a full pyramidal slip of $\frac{1}{3}[11\bar{2}\bar{3}]$ can be completed as shown in Fig. 3(c). Thus a full pyramidal slip of $\frac{1}{3}[11\bar{2}\bar{3}]$ can be obtained by

$$\frac{1}{6}[20\bar{2}\bar{3}] + \frac{1}{6}[0\bar{2}\bar{2}\bar{3}] \rightarrow \frac{1}{3}[11\bar{2}\bar{3}]$$

In this simulation, shearing due to a successive pyramidal $\langle a+c \rangle$ slip along the $\langle 11\bar{2}\bar{3} \rangle$ direction is responsible for deformation under the c -axis compression. No twinning with symmetrical structure has been found. A slip step appears at the surface of the sample after the slip moves out of the sample. Meanwhile, some interior defects are also left behind at the end of the shear region. This result is fully consistent with microcompression measurements of the single crystal magnesium in which no twinning was observed in the sample sizes from 2.1 to 10 μm under

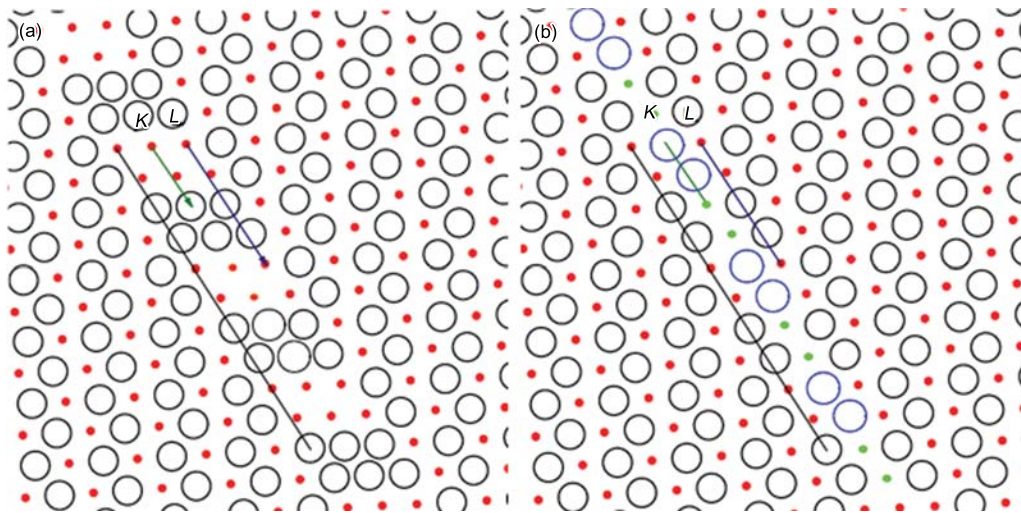


Fig. 4 Atomic arrangements in the slip bands: (a) only atoms movement projected in the $[\bar{1}2\bar{1}0]$ plane along the $[\bar{1}01\bar{2}]$ direction is represented; (b) the displacements along the $[\bar{1}2\bar{1}0]$ periodic direction is considered by exchanging the type of atoms along the plane K (that is, change black circles to green dots, and red dots to blue circles). The slip bands disappear in this plane representation and the configuration becomes a perfect hcp structure

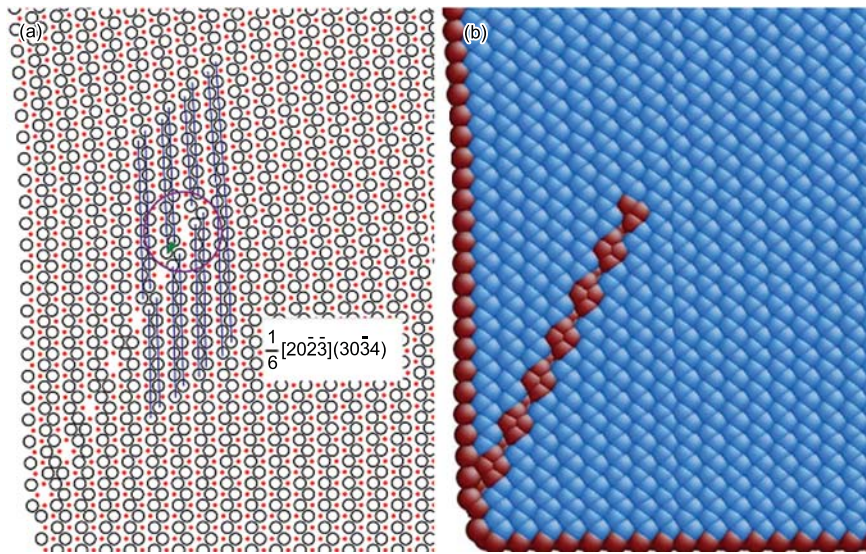


Fig. 5 Atomic arrangements of the stacking fault in a plane representation (a) and corresponding atoms identified by the CNA^[22] (b) (light blue is for perfect atoms, and red is for the stacking fault. At the end of the stacking fault, a $\frac{1}{6}[20\bar{2}\bar{3}]$ partial dislocation exists shown by the purple circle)

c-axis compression, and significant plasticity and hardening occurred due to six active pyramidal slip systems^[11,12].

3.2 Compression deformation of magnesium single crystal under different simulation conditions

Different loading and boundary conditions are applied in this section in order to compare with our simulation results in section 3.1. In section 3.1, we have observed that the defects are preferentially nucleated at the free surface of the simulation cell. To assess the effect of the free surface, the periodic boundary condition along the $[\bar{1}010]$ (*x*) direction is used. While a compression is applied in the *y* direction, a stretch is imposed in the *x* direction to avoid volume contraction due to the *c*-axis compression. Then the atoms are fully relaxed for 10000 steps. When the applied compression strain reaches 0.09, the slip bands begin to appear, which are just like the slip bands under the free-boundary condition (Fig. 2). No twinning is observed under this condition. It should be noted that no free surface exists in this sample due to the periodic boundary condition applied in both the *x* and *z* directions, the slip cannot initiate at the free surfaces. Therefore, the slip bands can only be observed at a compression strain higher than 0.09 in the sample under this periodic boundary condition.

Besides the effects of the boundary conditions we have also examined the effects of incremental loading mode by moving the boundary atoms in step-like fashion in performing our simulations. A compression strain along the $[0001]$ (*y*) direction is imposed in the sample by moving the boundary atoms and allowing the atoms to relax under fixed-displacement boundary condition. The compression strain of 0.002 is applied every 1000 steps, thus the strain rate is $3.33 \times 10^8 \text{ s}^{-1}$.

The compression and the relaxation process are repeated until the total compression strain has reached 0.104. In order to save computation time, a smaller system with dimensions $22 \text{ nm} \times 29 \text{ nm} \times 2.5 \text{ nm}$ containing 76800 atoms is used. As shown in Fig. 6 at strains of 0.08 and 0.104, the slip bands with the reorientation angle of about 90° are readily observed, while the slip bands with the reorientation angle of about 120° are also visible. These slip bands are caused by successive pyramidal $\langle a+c \rangle$ slips along the $\langle 11\bar{2}\bar{3} \rangle$ direction, just as those in Fig. 2. No twinning is observed in this simulation. At the higher strain level of 0.104, Fig. 6(b) shows an increase in the width of the shear regions as can be expected.

The corresponding stress-strain curve of *c*-axis compression for the strain rate of $3.33 \times 10^8 \text{ s}^{-1}$ is presented in Fig. 7. It is seen stress increases linearly with increasing strain during initial deformation. After the leading slip occurs at a strain of about 0.07, the stress drops off. Subsequently, with increasing strain, the stress begins to fluctuate due to initiation of slips and their interactions in different slip planes. Generally speaking high strain rates should favor deformation twinning. However, no twinning has been observed at different strain rates in our simulations. Dislocation plasticity governs the *c*-axis compression, as we have concluded from our static simulations.

All the deformation responses observed at the various temperatures and boundary conditions in the simulations have been checked and no symmetrical twin structure under *c*-axis compression was found. All the slip bands seen under compression are formed by successive $\langle a+c \rangle$ slips along the direction. No defect exists in these shear bands, and only the slip steps and the interior defects are left. Our simulation results therefore do not support the conventional expectation that deformation twinning should be the

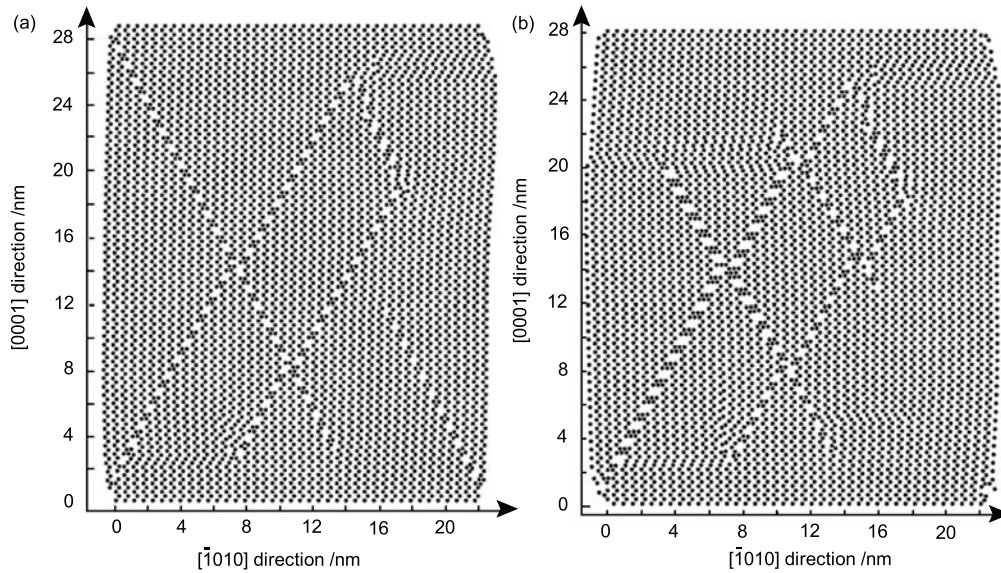


Fig. 6 Deformation of magnesium single crystal under c -axis compression in a step by step loading manner at 5 K with the applied compression strain of 0.08 (a) and 0.104 (b)

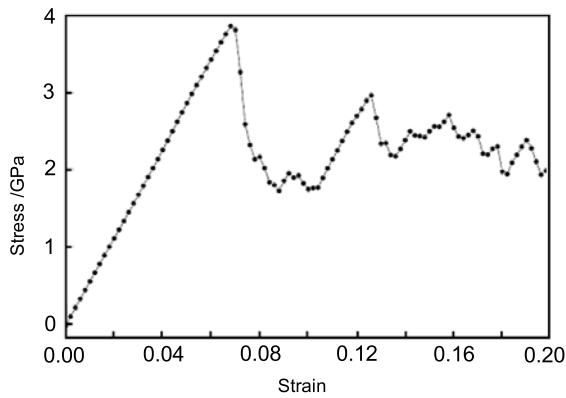


Fig. 7 The stress-strain curve of magnesium single crystal under c -axis compression in a step by step loading manner at 5 K

primary mechanism for c -axis compression in a bulk single crystal^[4,5].

3.3 Twinning deformation in pure magnesium single crystal

In previous works^[32,33], the twin deformation either in tension or compression is generally obtained by calculating the strain caused by the twinning shear. However, the twinning mechanism for the hcp metals is complicated and still subjected to discussion. For example, an atomic shuffling dominated mechanism was presented for the $\{10\bar{1}2\}$ twinning in magnesium, which suggested that the $\{10\bar{1}2\}$ twinning is achieved by the conversion of the basal planes to the prism planes^[21]. For the $\{10\bar{1}1\}$ twin, it was revealed that the atomic displacements as a twinning dislocation move can be described as a shear plus a series of shuffles^[23]. Thus the $\{10\bar{1}1\}$ twinning cannot be formed only by the $\langle 10\bar{1}2 \rangle$ shear. Some complicated atom movement (such as atoms shuffling)

should be considered for the $\{10\bar{1}1\}$ twinning, which finally causes the lattice rotation. So for the twinning in hcp metals, it is not enough to only consider the strain caused by the twinning shear.

Due to the mirror relationship in twinning, the twinned region is symmetrical to the original lattice about the twin plane, with no change of the crystal structure. Thus in our model, the detailed twinning mechanism is not considered because it is complicated. We calculate the strain only according to the symmetry of crystal structure after twinning. The lattice structure of an hcp crystal with c/a ratio of 1.623 has been previously shown in Fig. 1, along with two typical twin planes of $(10\bar{1}2)$ and $(10\bar{1}1)$ represented parallel to the $[\bar{1}2\bar{1}0]$ axis. Due to the periodic arrangement of atoms along the $[\bar{1}2\bar{1}0]$ direction, we give an idealized two-dimensional description of the $\{10\bar{1}2\}$ twin and the $\{10\bar{1}1\}$ twin in atomistic scale in Fig. 8. As we know for the metals with $c/a < \sqrt{3}$ (*e.g.* beryllium, titanium, zirconium, magnesium), the $\{10\bar{1}2\}$ twin is activated by c -axis tension with lattice rotation angle of 86.3° . After a rotation of 86.3° along the $[\bar{1}2\bar{1}0]$ axis, a typical $\{10\bar{1}2\}$ tension twin becomes symmetrical about the $(\bar{1}012)$ twin plane as can be seen in Fig. 8(a). We select two representative units M (in the original matrix) and N (in the twinned region), which are the elementary cells of the periodic structure in the $\{\bar{1}2\bar{1}0\}$ plane. The side lengths in unit M are $1.623a$ and $1.732a$, respectively, parallel and perpendicular to the c -axis direction. After $\{10\bar{1}2\}$ twinning, the long side in unit M transforms to the short side in unit N due to the rotation of about 90° . Therefore, the tensile strain that the $\{10\bar{1}2\}$ twin may accommodate can be approximately calculated as

$$\frac{1.732a - 1.623a}{1.623a} \approx 0.067$$

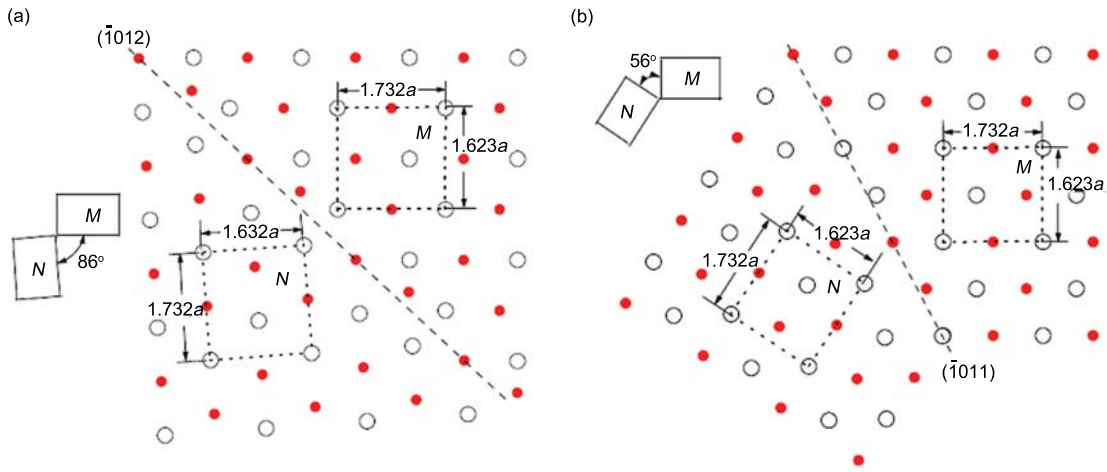


Fig. 8 Schematic of two typical twins in a $\{10\bar{1}2\}$ plane: (a) the $\{10\bar{1}2\}$ twin is symmetrical about the $(10\bar{1}2)$ twin plane; (b) the $\{10\bar{1}1\}$ twin is symmetrical about the $(10\bar{1}1)$ twin plane. Two representative units M in the original matrix and N in the twinned region are identified

If the tilting angle is considered to be of 86° , the tensile strain becomes slightly modified, as

$$0.067 \times \sin 86^\circ \approx 0.0668$$

This value is close to the value of 0.065 as the maximum tensile strain that twinning may accommodate according to Schmid and Boas^[34]. On the left side of Fig. 8(a), we give a simple structure scheme to describe this conversion. The ratio of side lengths is enlarged in this scheme to more clearly indicate the extension along the c -axis direction.

Fig. 8(b) shows a typical $\{10\bar{1}1\}$ twin symmetrical about the $(10\bar{1}1)$ twin plane. Compared to the $\{10\bar{1}2\}$ twin, the lattice rotation angle introduced by the $(10\bar{1}1)$ twinning is 56° . It is indicated in the upper-left structure scheme of Fig. 8(b), which is the same as the scheme in the left side of Fig. 8(a), that although the unit N is not vertical to unit M , the extension of the lattice unit N along the c -axis direction is obvious. Considering the tilting angle of unit N , the tensile strain that the $\{10\bar{1}1\}$ twin may accommodate can be estimated as

$$0.067 \times \sin 56^\circ \approx 0.0555$$

It follows that the ideal $\{10\bar{1}1\}$ twin in pure magnesium single crystal can accommodate the extension strain parallel to the c -axis. It means the $\{10\bar{1}1\}$ twinning prefers to occur under the c -axis tension due to the geometric compatibility. If only the strain caused by twinning is considered, both $\{10\bar{1}2\}$ and $\{10\bar{1}1\}$ twinning in magnesium single crystal are tension twins.

Based on above lattice-structure analysis, we may conclude that either $\{10\bar{1}2\}$ or $\{10\bar{1}1\}$ twinning can only accommodate extension strain parallel to the c -axis. When the c/a ratio of the hcp structure is less than $\sqrt{3}$, the representative unit M is a rectangle,

while the long side is perpendicular to the c -axis direction. After twinning, unit N in the twinned region, which is symmetrical to the original unit M about the twin plane, can only accommodate the extension strain parallel to the c -axis. Thus twinning is favored to occur under c -axis tension. The extension strain that the twin may accommodate varies with the rotation angle of the twin. However, if the crystal is loaded under the c -axis compression, no twinning will be favored to occur, and dislocation plasticity governs the compression deformation in pure magnesium single crystal. This explains why both $\{10\bar{1}2\}$ and $\{10\bar{1}1\}$ twinning have been observed in magnesium single crystal under c -axis tension by molecular dynamic simulations^[17]. It is also consistent with the conclusion that under c -axis compression in magnesium single crystal, the pyramidal $\langle a+c \rangle$ slip is the main deformation mechanism.

3.4 Discussion

The atomistic simulations and theoretical analysis presented here suggest that $\{10\bar{1}1\}$ twinning does not occur under c -axis compression in a single crystal. In previous simulation of deformation under c -axis tension, $\{10\bar{1}1\}$ twinning was indeed observed which conformed what one would expect^[24]. There is the belief that $\{10\bar{1}1\}$ twin should be a compression twin which is activated when there is a contraction strain component parallel to the c -axis^[4,5]. The simulation results and theoretical analysis in this work do not support this notion when applied to c -axis compression in a single crystal at the nanoscale. Several factors should be considered to interpret the implications.

This work is concerned with a pure magnesium single crystal without the complication associated with pre-existing defects, and structural inhomogeneities. This is far from the actual conditions of

sample specimens used in the existing experiments. For example, “compression twins” are generally observed in extruded or hot-rolled alloy specimens with different texture intensities and the grain sizes^[6,35]. In this condition, the initial orientation of the grains, a wide range of the grain boundaries, and the complicated stress states for the specimens have great influence on the deformation mechanism acting in magnesium and its alloys^[6,36–39]. Even in bulk single crystal measurements, pre-existing twins, low-angle boundaries and various other defects could be the activated sites for deformation twinning and thereby dictate the mechanisms initiating plasticity^[40]. Still another consideration is that alloy elements can have considerable influence on deformation behavior, including the structure and size of the lattice. Therefore, the ideal condition of pure magnesium crystal sample, as presented in our simulation and theoretical analysis, is difficult to obtain in experiments.

Besides the complications of materials inhomogeneities, experimental stress states are more complicated than simple compression or tension. For extruded or hot-rolled alloys with the anisotropy and texture, compressive tests are performed in these specimens since the majority of the grains are compressed along their *c*-axis and expand in the perpendicular direction. Because of grain-orientation variation, one cannot ensure that all the grains in the sample are in fact subjected to compression. Therefore, $\{10\bar{1}1\}$ twinning could occur within the grains start out with very different initial orientations and some subjected to local tensile stress states in the samples during the process of overall compression. Even in channel die testing compression experiments^[4,5] for the magnesium single crystals, non-uniaxiality and friction may cause variation of the local stress states leading to nucleation of twinning^[11].

Recent measurements of magnesium (0001) single crystal showed that no twinning is observed in the sample sizes from 2.1 to 10 μm under *c*-axis compression^[11,12]. These findings are quite consistent with our work in which the $\{10\bar{1}1\}$ twinning is not observed in pure magnesium single crystals under *c*-axis compression. Additionally, it was found in titanium single crystal that for crystal sample size below 1 μm deformation twinning was entirely replaced by dislocation plasticity^[13]. Thus both microcompression for magnesium single crystal and situ nano-compression on for titanium revealed a strong crystal size effect on deformation twinning, supporting our findings that at the nanoscale deformation twinning is not the primary deformation mechanism in a ideal pure hcp single crystal. Furthermore, these experiment results show the a “loss” of twins in some cold rolled magnesium alloys, and the shear bands dominate the rolling deformation^[9]. This also gives an evidence to support our results that dislocation plasticity governs *c*-axis compression. In other words, twinning should not be dominant in compression response when the *c/a* ratio

of the hcp metal is smaller than $\sqrt{3}$.

4. Conclusions

Molecular dynamics simulations are applied to study the compression deformation behavior in magnesium single crystal under different simulation conditions. The result shows that pyramidal $\langle a + c \rangle$ slip is the main deformation mechanism under *c*-axis compression at the nanoscale. No compression twins are observed. Further analysis of the lattice structure reveals that twinning can only accommodate extension strain parallel to the *c*-axis when the *c/a* ratio of the hcp structure is less than $\sqrt{3}$. Thus compression twins will not occur in pure magnesium single crystal at the nanoscale. Our result is supported by recent micro-compression experiments on magnesium (0001) single crystals that dislocation plasticity governs *c*-axis compression.

Acknowledgements

This work was supported by the National Natural Science Foundation of China (Nos. 11072026 and 10632020) and the Fundamental Research Funds for the Central Universities (No. 2009JBZ015). The Authors gratefully acknowledge D. Steglich, B. Yildiz and Y. Fan for useful discussions. Yafang GUO acknowledges the hospitality of the Nuclear Science and Engineering Department at MIT during a sabbatical visit.

REFERENCES

- [1] C.S. Roberts, *Magnesium and Its Alloys*, Wiley, New York, 1960, pp. 81–107.
- [2] M.M. Avedesian and H. Baker, *Magnesium and Magnesium Alloys*, ASM Specialty Handbook, ASM International, Materials Park, Ohio, 1999, pp. 3–84.
- [3] M.R. Barnett, *Mater. Sci. Eng. A* **464** (2007) 1.
- [4] E.W. Kelley and W.F. Hosford, *Trans. Metall. Soc. AIME*. **242** (1968) 5.
- [5] R.E. Reed-Hill, and W.D. Robertson, *Acta Metall.* **5** (1957) 717.
- [6] M.D. Nave and M.R. Barnett, *Scr. Mater.* **51** (2004) 881.
- [7] W.H. Hartt and R.E. Reed-Hill, *Trans. Metall. Soc. AIME*. **242** (1968) 1127.
- [8] M.M. Myshlyayev, H.J. McQueen, A. Mwembela and E. Konopleva, *Mater. Sci. Eng. A* **337** (2002) 121.
- [9] M.R. Barnett, M.D. Nave and C.J. Bettles, *Mater. Sci. Eng. A* **386** (2004) 205.
- [10] S.L. Couling, J.F. Pashak and L. Sturkey, *Trans. ASM*. **51** (1959) 94.
- [11] E. Lilleodden, *Scr. Mater.* **62** (2010) 532.
- [12] C.M. Byer, B. Li, B. Cao and K.T. Ramesh, *Scr. Mater.* **62** (2010) 536.
- [13] Q. Yu, Z.W. Shan, J. Li, X. Huang, L. Xiao, J. Sun and E. Ma, *Nature* **463** (2010) 335.
- [14] F. Cleri, D. Wolf, S. Yip, S.R. Phillpot, *Acta Mater.* **45** (1997) 4993.
- [15] M.J. Buehler, F.F. Abraham and H. Gao, *Nature* **426** (2003) 141.

- [16] S.J. Zhou, D.L. Preston, P.S. Lomdahl and D. M. Beazley, *Science* **279** (1998) 1525.
- [17] J.Knap and K. Sieradzki, *Phys. Rev. Lett.* **82** (1999) 1700.
- [18] Y.F. Guo, Y.S. Wang, D.L. Zhao and W. P. Wu, *Acta Mater.* **55** (2007) 6634.
- [19] J.Schiøtz, F.D.D. Tolla and K.W. Jacobsen, *Nature* **391** (1998) 561.
- [20] J.Wang, J.P. Hirth and C.N. Tomé, *Acta Mater.* **57** (2009) 5521.
- [21] B. Li and E. Ma, *Phys. Rev. Lett.* **103** (2009) 035503.
- [22] A. Serra, R.C. Pond and D.J. Bacon, *Acta Metall. Mater.* **39** (1991) 1469.
- [23] J. Wang, I.J. Beyerlein, J.P. Hirth and C.N. Tomé, *Acta Mater.* **59** (2011) 3990.
- [24] Y.F. Guo, Y.S. Wang, H.G. Qi and D. Steglich, *Acta Metall. Sin. (Engl. Lett.)* **23** (2010) 370.
- [25] X.Y. Liu, J.B. Adams, F. Ercolessi and J.A. Moriarty, *Modell. Simul. Mater. Sci. Eng.* **4** (1996) 293.
- [26] D.L. Olmsted, Jr. L.G. Hector and W.A. Curtin, *J. Mech. Phys. solids* **54** (2006) 1763.
- [27] J. Riffkin, XMD-Molecular Dynamics for Metals and Ceramics, Available from: <http://xmd.sourceforge.net/>.
- [28] D. Faken and H. Jónsson, *Comput. Mater. Sci.* **2** (1994) 279.
- [29] J. Schiøtz, *Scr. Mater.* **51** (2011) 837.
- [30] B. Schonfelder, G. Gottstein and L.S. Shvindlerman, *Acta Mater.* **53** (2005) 1597.
- [31] Z.L. Pan, Y.L. Li and Q. Wei, *Acta Mater.* **56** (2008) 3470.
- [32] R.W. Hertzberg, *Deformation and Fracture Mechanics of Engineering Materials*, Fourth Edition, John Wiley & Sons, Inc., New York, 1996, pp. 113–116.
- [33] M.H. Yoo, *Metall. Tran. A* **12** (1981) 409.
- [34] E. Schmid and W. Boas, *Kristallplastizität*, Julius Springer, Berlin, 1935, p. 1
- [35] Y. Chino, K.Kimura, M.Hakamada and M.Mabuchi, *Mater. Sci. Eng. A* **485** (2008) 311.
- [36] A. Staroselsky and L. Anand, *Int. J. Plast.* **19** (2003) 1843.
- [37] S.R. Agnew and O. Duygulu, *Int. J. Plast.* **21** (2005) 1161.
- [38] L. Jiang, J.J. Jonas, A.A. Luo, A.K. Sachdev and S. Godet, *Scr. Mater.* **54** (2006) 771.
- [39] S.B. Yi, C.H.J. Davies, H.G. Brokmeier, R.E. Bolmaro, K.U. Kainer and J.Homeyer, *Acta Mater.* **54** (2006) 549.
- [40] J. Ye, R.K. Mishra, A.K. Sachdev and A.M. Minor, *Scr. Mater.* **64** (2011) 292.